PAPER

Check for updates

Enhanced acetylene semi-hydrogenation on a subsurface carbon tailored Ni–Ga intermetallic catalyst†

Xiaohu Ge,‡[a] Zhouhong Ren,‡[b] Yueqiang Cao, [ID] *[a] Xi Liu, [ID] [b] Jing Zhang,[a] Gang Qian,[a] Xueqing Gong, [ID] [c] Liwei Chen,[b] Xinggui Zhou,[a] Weikang Yuan[a] and Xuezhi Duan [ID] *[a]

Tailoring the active sites to promote the formation of the target product is of great importance for selective hydrogenations catalyzed by non-noble metals but remains challenging. Herein, we propose to employ carbon atoms to be incorporated into the Ni_3Ga intermetallic with partially isolated Ni sites aiming to enhance the catalytic performances for acetylene semi-hydrogenation. The incorporation of carbon atoms into the lattice of the Ni_3Ga intermetallic is achieved by thermal processing of the Ni_3Ga intermetallic catalyst in an acetylene atmosphere. The processed catalyst is proven to show the typical $Ni_3GaC_{0.5}$ phase by multiple characterization techniques including atomic-resolution electron microscopy and X-ray absorption spectroscopy. The presence of subsurface carbon in the $Ni_3GaC_{0.5}$ catalyst is experimentally and theoretically demonstrated to synergize with Ga sites for modifying the electronic structures of Ni *via* obvious hybridization of Ni 3d with Ga 2p and C 2p orbitals. The performance tests show that the $Ni_3GaC_{0.5}$ catalyst delivers high ethylene selectivity, up to *ca.* 90% at full conversion of acetylene, which outperforms the referred Ni and Ni_3Ga catalysts. The excellent selectivity to ethylene is rationalized by theoretical calculations, which point out that the desorption of ethylene from the $Ni_3GaC_{0.5}$ catalyst is kinetically more favourable than its hydrogenation to ethane. In addition, the stability of the $Ni_3GaC_{0.5}$ catalyst is also enhanced against the Ni and Ni_3Ga catalysts due to the suppressed formation of C_4 products.

[a]State Key Laboratory of Chemical Engineering, East China University of Science and Technology, 130 Meilong Road, Shanghai 200237, China. E-mail: yqcao@ecust.edu.cn; xzduan@ecust.edu.cn

[b]School of Chemistry and Chemical Engineering, In-situ Center for Physical Sciences, Frontiers Science Center for Transformative Molecules, Shanghai Jiao Tong University, Shanghai 200240, China

[c]Key Laboratory for Advanced Materials, Centre for Computational Chemistry and Research Institute of Industrial Catalysis, East China University of Science and Technology, 130 Meilong Road, Shanghai 200237, China

† Electronic supplementary information (ESI) available. See https://doi.org/10.1039/d2ta02216h

‡ These authors contributed equally to this work.

Xuezhi Duan received his PhD degree in Chemical Engineering from East China University of Science and Technology (ECUST) in 2012. After a two-year (2013–2015) stint as a post-doctoral fellow at Norwegian University of Science and Technology, he joined the faculty of School of Chemical Engineering at ECUST. He is a full professor and deputy director of the State Key Laboratory of Chemical Engineering. His current research interests include kinetics-assisted catalyst design, theoretical calculations and reactor engineering. In addition, he received the Young Scientist Prize awarded by the International Association of Catalysis Societies, the Outstanding Youth Award of Global Chinese Chemical Engineers Symposium, the Henry Fok Youth Teacher Award, the Chinese Chemical Society Young Chemist Award, etc.

19722 | *J. Mater. Chem. A*, 2022, **10**, 19722–19731

This journal is © The Royal Society of Chemistry 2022

1. Introduction

Heterogeneous catalysis for selective hydrogenation is enormously significant for producing both bulk chemicals and fine chemicals in industry, such as the catalytic acetylene semi-hydrogenation used for purifying the ethylene product from the naphtha cracking process.[1–3] Catalysts that have achieved some extent of success are made up of noble metals, and, currently, the commercial catalyst employed in the reaction is alumina supported Pd-based catalysts.[4,5] Considering the high cost/low abundance of noble metals, catalysts consisting of non-noble metals with excellent catalytic performances are needed in the efforts to improve the hydrogenation process. Along this line, Ni-based catalysts have received considerable interest for acetylene semi-hydrogenation, yet they suffer from the imperfect selectivity to the target ethylene, especially at high conversion of acetylene, owing to the unfavourable desorption of ethylene and its facile hydrogenation.[1,6–10] Therefore, construction of Ni active sites showing remarkably predominant ethylene desorption over ethylene hydrogenation is a goal in the pursuit of designing excellent Ni-based catalysts for acetylene semi-hydrogenation but it still remains challenging to date.

Introducing another metal to alloy with Ni is widely employed as a strategy for regulating the Ni active sites *via* the so-called geometric and electronic effects.[1,4,6,8,10–16] Recently, intermetallic catalysts featuring stable structures and long-range ordering atomic arrangement were proposed as promising candidate catalysts for acetylene semi-hydrogenation.[11,12,14,17,18] Regulating Ni sites with the guest metal sites to the completely isolated ones in intermetallic structures is an effective approach to suppress the strong σ-adsorption mode while it favors the weak π-adsorption for ethylene, which promotes the ethylene desorption and suppresses its hydrogenation to ethane.[8,17,18] However, the adsorption modes for acetylene and ethylene are still σ-adsorption for Ni-/Pd-based intermetallic catalysts with partially isolated Ni/Pd active sites.[2,5–8,16–25] These features give rise to unfavorable selectivity to ethylene but relatively higher hydrogenation activity in comparison with the intermetallic catalysts with completely isolated Ni/Pd sites. An interesting challenge that arises is addressing the possibility of further optimizing the adsorption/desorption behaviors of ethylene on such partially isolated active sites toward excellent ethylene selectivity, which could also maintain the relatively higher activity than the completely isolated active sites.

Considering that introducing another guest metal to the host metal expands the lattice of the host metal, it is of great interest to incorporate light atoms with a small radius into the expanded lattice of intermetallics to tailor the electronic and geometric structures of active sites. For acetylene semi-hydrogenation, light atoms, such as carbon and lithium, located inside the lattice of active metals have been well illustrated to remarkably improve the catalytic performances, especially the selectivity to ethylene.[6,26–28] In this work, we propose to employ carbon atoms to be incorporated into the Ni₃Ga intermetallic with partially isolated Ni sites aiming to tailor the catalytic performances for acetylene semi-hydrogenation. The Ni₃Ga intermetallic catalyst was synthesized using quaternary Ni/Ga/Mg/Al layered double hydroxides (LDHs) as the precursor. The synthesized Ni₃Ga catalyst was then processed in an acetylene atmosphere at 300 °C to introduce carbon atoms into the lattice of the Ni₃Ga intermetallic. The structural features of the processed catalyst were identified by multiple techniques including atomic-resolution electron microscopy and X-ray absorption spectroscopy, which reveal the formation of the $Ni_3GaC_{0.5}$ phase. The presence of carbon at the interstitial sites of Ni₃Ga has been experimentally and theoretically proven to obviously change the electronic properties of Ni sites. Catalytic performance tests show that the $Ni_3GaC_{0.5}$ catalyst exhibits excellent ethylene selectivity up to *ca.* 90% at 100% acetylene conversion, significantly prevailing over the referred Ni₃Ga and Ni catalysts. Density functional theory (DFT) calculations were used to rationalize the origin of enhancement of the subsurface carbon atoms on the Ni₃Ga intermetallic for the reaction.

2. Methods

2.1 Synthesis of catalysts

Quaternary Ni/Ga/Mg/Al-LDHs was fabricated by a facile co-precipitation method. Typically, 2.12 g of Na_2CO_3 was dissolved in 50 mL of ultra-pure water to form a homogeneous solution denoted as A. Then, 1.45 g of $Ni(NO_3)_2 \cdot 6H_2O$, 6.41 g of $Mg(NO_3)_2 \cdot 6H_2O$, 0.69 g of $Ga(NO_3)_3 \cdot xH_2O$ and 3.13 g of $Al(NO_3)_3 \cdot 9H_2O$ were dissolved in 50 mL of ultra-pure water to obtain a mixed metal salt solution denoted as B. 5.00 g of NaOH was subsequently dissolved in 125 mL of ultra-pure water as another alkali solution denoted as C. Then, solutions B and C were simultaneously added dropwise into solution A at 65 °C under vigorous stirring, during which the pH of the mixed solution was maintained at 10. Thereafter, the resulting coprecipitation product was aged at 65 °C for 18 h under vigorous stirring, and then was filtered and washed with excessive water until the pH of the washing solution reached around 7. After being dried at 100 °C for 18 h in static air, the obtained solid sample was completely ground, and then soaked in a solution of Na_2CO_3 for 16 h. The mixture was filtered and washed several times with excessive water to remove basic residues. Finally, the quaternary Ni/Ga/Mg/Al-LDHs was obtained after drying at 120 °C for 16 h. For comparison, the ternary Ni/Mg/Al-LDHs was also synthesized using a procedure similar to that of Ni/Ga/Mg/Al-LDHs without the addition of $Ga(NO_3)_3 \cdot xH_2O$. The synthesized Ni/Mg/Al-LDHs and Ni/Ga/Mg/Al-LDHs were reduced at 900 °C for 4 h to obtain the corresponding Ni and Ni₃Ga catalysts, respectively. The Ni₃Ga catalyst was processed in a 1.0% C_2H_2/N_2 atmosphere at 300 °C for 3 h to synthesize the $Ni_3GaC_{0.5}$ catalyst.

2.2 Characterizations of the materials

X-ray diffraction (XRD) patterns were collected on a D8 ADVANCE diffractometer with Cu Kα radiation working at 40 kV

This journal is © The Royal Society of Chemistry 2022

J. Mater. Chem. A, 2022, **10**, 19722–19731 | **19723**

and 40 mA. For the time-resolved XRD measurements, the reduced Ni_3Ga intermetallic catalyst was treated with 1.0% C_2H_2/N_2 at 300 °C for 160 min, and the XRD patterns were simultaneously recorded every twenty minutes. The high-resolution transmission electron microscopy (HRTEM) images and high-angle annular dark field scanning transmission electron microscopy (HAADF-STEM) images were obtained using a JEOL JEM-2010 F transmission electron microscope. Aberration-corrected HAADF-STEM (AC-HAADF-STEM) analysis was performed on a Hitachi HF5000 scanning transmission electron microscope with a Cs corrector operating at 200 kV. X-ray photoelectron spectroscopy (XPS) spectra were recorded on a Thermo Scientific ESCALAB 250xi system equipped with Al Kα radiation. The corresponding binding energies of samples were calibrated by employing the C 1s peak (284.6 eV) as a reference. XAFS measurements at the Ni K edge (8333 eV) were carried out at the BL11B XAFS beamline of the Shanghai Synchrotron Radiation Facility (SSRF). The specific composition of green oil was characterized by pyrolysis GC-MS (Agilent 7890A GC/5975C MSD) with an HP-5MS column, as clearly described in our previous work.[5,29] The thermogravimetric characterizations were performed using a PerkinElmer Pyris 1 at a heating rate of 5 °C min^{-1} from 20 to 800 °C.

2.3 Acetylene hydrogenation testing

The catalytic performances of the Ni, Ni_3Ga and $Ni_3GaC_{0.5}$ catalysts were evaluated in a tubular stainless steel reactor. About 150 mg of the catalyst sample diluted with 400 mg quartz sand was loaded into the center of the reactor tube and reduced in 40 vol% H_2/N_2 with a certain gas flow rate at 800 °C for 3 h. After cooling down the temperature to the reaction temperature, the feed gas composed of 0.5 vol% acetylene, 2.5 vol% hydrogen, 10.0 vol% ethylene and the rest N_2 was introduced into the reactor at a flow rate of 100 mL min^{-1}. The compositions of the inlet and outlet streams were analyzed online using a gas chromatograph (INFICON 3000 Micro) equipped with TCD detectors. The acetylene conversion and ethylene selectivity were calculated as follows:

$$C_2H_2 \text{ conversion} = \frac{C_2H_2 \text{ (inlet)} - C_2H_2 \text{ (outlet)}}{C_2H_2 \text{ (inlet)}} \times 100\%$$

$$S(C_2H_4) = \left\{ 1 - \frac{C_2H_6 \text{ (outlet)} - C_2H_6 \text{ (inlet)}}{C_2H_2 \text{ (inlet)} - C_2H_2 \text{ (outlet)}} - \frac{2 \times [C_4 \text{ (outlet)} - C_4 \text{ (inlet)}]}{C_2H_2 \text{ (inlet)} - C_2H_2 \text{ (outlet)}} \right\} \times 100\%$$

$$S(C_2H_6) = \frac{C_2H_6 \text{ (outlet)} - C_2H_6 \text{ (inlet)}}{C_2H_2 \text{ (inlet)} - C_2H_2 \text{ (outlet)}} \times 100\%$$

$$S(C_4) = \frac{2 \times [C_4 \text{ (outlet)} - C_4 \text{ (inlet)}]}{C_2H_2 \text{ (inlet)} - C_2H_2 \text{ (outlet)}} \times 100\%$$

At the conversion of *ca.* 10%, the carbon differences were both less than 1.0% for the Ni, Ni_3Ga and $Ni_3GaC_{0.5}$ catalysts; at the conversion of *ca.* 90%, the carbon differences were 6.0, 4.5 and 2.0% for Ni, Ni_3Ga and $Ni_3GaC_{0.5}$ catalysts, respectively. The higher carbon differences for the Ni and Ni_3Ga catalysts suggest that more carbonaceous compounds were formed on the catalysts.

2.4 DFT calculations

All DFT calculations were carried out using the well-established Vienna *Ab initio* Simulation Package (VASP)[30–32] with plane wave basis sets and projected-augmented wave (PAW) pseudopotentials.[33] The generalized gradient approximation (GGA) proposed by Perdew–Burke–Ernzerhof (PBE)[34] was applied to explicitly describe the exchange–correlation functionals. The Ni(111), Ni_3Ga(111), $Ni_3GaC_{0.5}$(111), Ni_3Ga(200) and $Ni_3GaC_{0.5}$(200) surfaces were employed for DFT calculations. Ni(111), Ni_3Ga(111) and Ni_3Ga(200) surfaces were modeled with four layers in p(2 × 2) supercells. $Ni_3GaC_{0.5}$(111) and $Ni_3GaC_{0.5}$(200) surfaces were modeled with two layers in the p(1 × 1) supercell. For Ni(111), Ni_3Ga(111) and Ni_3Ga(200) surfaces, the top two layers were relaxed, and the others were fixed at the bulk lattice positions. For $Ni_3GaC_{0.5}$(111) and $Ni_3GaC_{0.5}$(200) surfaces, the first layer was allowed to relax, and the second was fixed at the bulk lattice positions. A vacuum layer thickness of 20 Å was added between the periodically repeated slabs to prevent interactions from adjacent cells. The transition states corresponding to elementary steps of acetylene hydrogenation were located by the dimer method[35] and checked by the vibrational frequency analysis to ensure only one imaginary frequency. Bader analysis[36] was performed to determine atomic electronic charges for studying electronic interaction difference after introducing subsurface C species into the Ni_3Ga intermetallic phase.

3. Results and discussion

Fig. 1a presents the XRD patterns of the monometallic Ni and intermetallic Ni_3Ga catalysts, in which the characteristic

Fig. 1 (a) XRD patterns of Ni and Ni_3Ga catalysts. (b) Time-resolved XRD contour maps of the Ni_3Ga catalyst under 1.0% C_2H_2/N_2 at 300 °C, where the schematic diagram of the phase transformations from the intermetallic Ni_3Ga phase into the $Ni_3GaC_{0.5}$ phase is shown in the inset.

19724 | *J. Mater. Chem. A*, 2022, **10**, 19722–19731

This journal is © The Royal Society of Chemistry 2022

diffraction peaks observed at 36.8°, 59.3° and 65.2° are assigned to the reflections of (311), (511) and (400) planes of the cubic $MgAl_2O_4$ phase (JCPDS No. 21-1152), respectively, and the diffraction peaks at 42.9° and 62.3° are indexed to the (200) and (220) reflections of cubic MgO (JCPDS No. 45-0946), respectively. In addition to these characteristic peaks of the support, the XRD pattern of the Ni catalyst shows obvious diffraction peaks at 44.3°, 51.7° and 76.1° ascribed to the crystalline planes (111), (200) and (220) of the face-centred cubic (FCC) Ni phase (JCPDS No. 65-0380),[8,15,26] respectively. In contrast, the pattern of the intermetallic Ni_3Ga catalyst exhibits three diffraction peaks at 43.7°, 50.9° and 74.9° attributed to the (111), (200) and (220) planes of the Ni_3Ga intermetallic phase with an FCC crystal structure (JCPDS No. 65-8294), respectively. These experimental XRD patterns also match well with the simulated ones of the Ni and Ni_3Ga FCC crystals (Fig. S1†).

Based on the Ni_3Ga catalyst, the subsurface carbon modified Ni_3Ga catalyst was synthesized by processing with the C_2H_2 reactant at 300 °C, in which the phase transformation from Ni_3Ga into $Ni_3GaC_{0.5}$ was identified by the time-resolved XRD measurements shown in Fig. 1b. The peak at 43.7° assigned to Ni_3Ga(111) shifts gradually to smaller diffraction angles on increasing the processing time during the process, suggesting the incorporation of C atoms into the lattice of Ni_3Ga.[6,26,37] After processing for 160 min, the XRD pattern in the ESI, Fig. S2† demonstrates the complete formation of the $Ni_3GaC_{0.5}$ phase (JCPDS No. 29-0625), and thus the formed catalyst is denoted as $Ni_3GaC_{0.5}$. A similar process was also carried out for the mono-metallic Ni catalyst. In contrast, no obvious diffraction peaks corresponding to the Ni_3C phase (JCPDS No. 01-7005) were observed from the XRD pattern for the processed Ni catalyst as shown in the ESI, Fig. S3,† indicating the absence of carbon atoms incorporated into the Ni lattice. Instead, the dissociated carbon atoms from acetylene molecules prefer to assemble on the monometallic Ni surface to form carbon nanofibers,[6,26] which is also confirmed by the SEM images in the ESI, Fig. S4.† This could be caused by the limited space available for the dissolved carbon atoms at the Ni octahedral site (Fig. S5†), which leads to easier segregation of carbon atoms onto the surface.[6]

High resolution transmission electron microscopy (HRTEM) and high angle annular dark-field scanning transmission electron microscopy (HAADF-STEM) were further performed to reveal the detailed microstructural features of the synthesized Ni, Ni_3Ga and $Ni_3GaC_{0.5}$ catalysts. Fig. S6†, 2a and b display the typical HRTEM images with the corresponding fast Fourier transform (FFT) patterns of Ni, Ni_3Ga and $Ni_3Ga_{0.5}$, respectively. The interplanar spacing of lattice fringes in the ESI, Fig. S6† is determined to be 0.204 nm, which is ascribed to the interplanar spacing of the Ni(111) plane. Similarly, the averaged spacing of lattice fringes in the HRTEM image of the Ni_3Ga catalyst is measured to be around 0.206 nm, agreeing well with the interplanar spacing of the Ni_3Ga(111) plane. In contrast, the interlayer lattice spacing is determined to be 0.212 nm for $Ni_3GaC_{0.5}$ catalyst, which is assigned to the (111) plane of the $Ni_3GaC_{0.5}$ phase (JCPDS No. 29-0625). Clearly, the lattice of the $Ni_3GaC_{0.5}$ catalyst is expanded as compared to that of the Ni_3Ga catalyst, demonstrating the presence of C atoms located in the

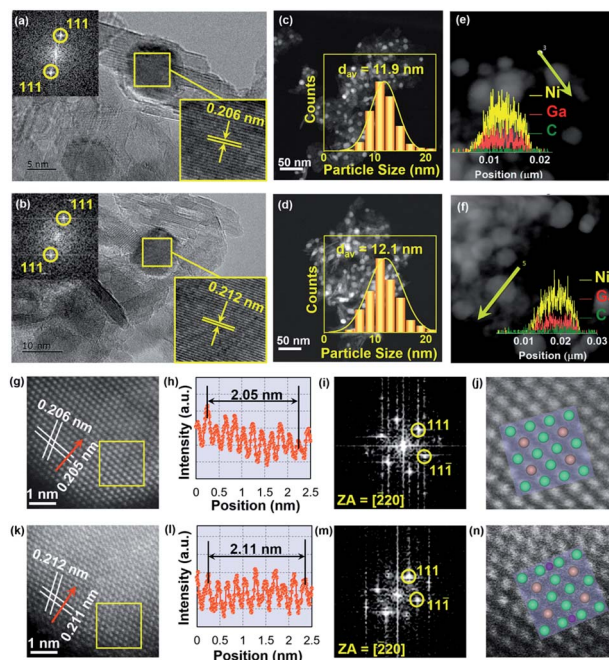**Fig. 2** HRTEM images of (a) Ni_3Ga and (b) $Ni_3GaC_{0.5}$ catalysts. The insets are the corresponding FFT patterns. HAADF-STEM images of (c and e) Ni_3Ga and (d and f) $Ni_3GaC_{0.5}$ catalysts. Insets in (c) and (d) are the corresponding histograms of the particle size distributions, and those in (e) and (f) are the corresponding EDS line-scanning profiles. (g) Representative AC-HAADF-STEM images of the Ni_3Ga catalyst. (h) Line intensity profiles along the direction marked by the red arrows in (g). (i) FFT patterns of the Ni_3Ga catalyst. (j) Enlarged views of the areas marked by the yellow rectangles in (g) and the corresponding crystal structure models along with [$\bar{2}20$] zones. (k) Representative AC-HAADF-STEM images of the $Ni_3GaC_{0.5}$ catalyst. (l) Line intensity profiles along the direction marked by the red arrows in (k). (m) FFT patterns of the $Ni_3GaC_{0.5}$ catalyst. (n) Enlarged views of the areas marked by the yellow rectangles in (k) and the corresponding crystal structure models along with [$\bar{2}20$] zones.

Ni_3Ga crystal lattice. Moreover, no carbonaceous carbon is observed on the $Ni_3GaC_{0.5}$ particle, indicating that the expanded lattice of Ni_3Ga (Fig. S5†) as compared to that of Ni is more favorable for stabilizing carbon atoms at the larger octahedral site.[6] Furthermore, the Ni, Ni_3Ga and $Ni_3GaC_{0.5}$ nanoparticles are uniformly distributed on the catalysts, as shown in the HAADF-STEM images (Fig. S7†, 2c and d), and the measured average nanoparticle sizes of Ni, Ni_3Ga and $Ni_3GaC_{0.5}$ are 12.3, 11.9 and 12.1 nm, respectively. These similar particle sizes enable one to unravel the synergetic effects of surface Ga and subsurface C atoms on Ni active sites by excluding the particle size effects on acetylene hydrogenation. The energy dispersive X-ray spectroscopy (EDS) line-scanning within a single nanoparticle for the Ni_3Ga catalyst shows that Ni and Ga elements are uniformly distributed over the particle (Fig. 2e), which is consistent with the EDS mapping analysis in the ESI, Fig. S8.† For the $Ni_3GaC_{0.5}$ catalyst, as seen in the EDS line-scanning in Fig. 2f, the Ni, Ga and C elements are also homogeneously distributed over the entire $Ni_3GaC_{0.5}$ nanoparticle, agreeing well with the EDS mapping analysis in the ESI, Fig. S9.† These

This journal is © The Royal Society of Chemistry 2022

J. Mater. Chem. A, 2022, **10**, 19722–19731 | **19725**

results indicate the successful fabrication of Ni_3Ga and $Ni_3GaC_{0.5}$ structures. Similarly, the EDS line-scanning and mapping analysis for the monometallic Ni catalyst shown in the ESI, Fig. S10 and S11† demonstrate the uniform spatial distribution of Ni element and the absence of Ga and C elements.

The atomic-scale structures of the Ni_3Ga and $Ni_3GaC_{0.5}$ catalysts were further revealed by AC-HAADF-STEM techniques. The typical AC-HAADF-STEM image of the Ni_3Ga catalyst in Fig. 2g displays the well-defined arrangement of Ni and Ga atoms in a rhombic periodic arrangement throughout the whole nanoparticle. As shown in Fig. 2h, the line intensity profile along with the red arrow marked in Fig. 2g illustrates that the lattice spacing along this direction is 0.205 nm, close to that of the (111) plane of the $Pm\bar{3}m$ Ni_3Ga intermetallic phase. In addition, the atomic arrangement predicted by the crystal structural models along with the $[\bar{2}20]$ zone axis, which is determined by the FFT pattern (Fig. 2i) for the region marked by the yellow rectangle in Fig. 2g, is in good agreement with that experimentally observed by AC-HAADF-STEM in Fig. 2j. The AC-HAADF-STEM image of the $Ni_3GaC_{0.5}$ catalyst in Fig. 2k shows the well-defined ordered atomic arrangement with clear lattice fringes. The integrated pixel intensity profile (Fig. 2l) taken from the red arrow marked in Fig. 2k reveals that the average spacing of the lattice fringe is 0.211 nm, which is assigned to the $Ni_3GaC_{0.5}$(111) plane. Furthermore, the predicted atomic distribution of $Ni_3GaC_{0.5}$ along with the $[\bar{2}20]$ zone axis determined by the corresponding FFT pattern (Fig. 2m) for the yellow rectangle region in Fig. 2k matches well with the observed one in Fig. 2n. These results unequivocally show the atomically ordered structure of intermetallic Ni_3Ga and that of the carbon doped one (*i.e.*, $Ni_3GaC_{0.5}$).

To unravel the electronic interaction between Ni, Ga and C, XPS analysis was employed to identify the electronic structures of Ni, Ni_3Ga and $Ni_3GaC_{0.5}$ catalysts. The satellite peaks at the binding energy of 861.9 eV seen in the Ni 2p XPS spectrum of the monometallic Ni catalyst are ascribed to multielectron excitation (Fig. 3a).[38] Besides, the two peaks centred at binding

energies of 852.9 and 855.7 eV are attributed to Ni^0 and Ni^{2+} species, respectively. In contrast, the Ni 2p peaks of the Ni_3Ga catalyst shift towards lower binding energy by 0.51 eV compared with those of the Ni catalyst, revealing the visible electron transfer from Ga to Ni in the Ni_3Ga intermetallic structure due to the higher electronegativity of Ni (1.91) than that of Ga (1.81).[8] Notably, the Ni 2p peaks of the $Ni_3GaC_{0.5}$ catalyst show an evident shift to higher binding energy by 0.46 eV as compared with those of the Ni_3Ga catalyst. Meanwhile, the binding energy of the Ga 2p XPS spectrum of the $Ni_3GaC_{0.5}$ catalyst is close to that of the Ni_3Ga catalyst in Fig. 3b, which implies that the electrons are transferred from Ni atoms to C ones after introducing C atoms into the lattice of the intermetallic Ni_3Ga. It should be noted that the presence of the Ni^{2+} and Ga^{3+} species is reasonably related to the re-oxidation of the sample during the *ex situ* tests.[5,8] The normalized X-ray absorption near-edge structure (XANES) spectrum at the Ni K-edge was further employed to reveal the electronic structures of the Ni, Ni_3Ga and $Ni_3GaC_{0.5}$ catalysts. As shown in Fig. 3c, the energy of the adsorption edge of the $Ni_3GaC_{0.5}$ catalyst shifts to higher position compared with that of the Ni_3Ga catalyst. This demonstrates the electron-deficient character of the Ni atoms in the $Ni_3GaC_{0.5}$ catalyst due to the considerable electron transfer from Ni atoms to the adjacent C atoms,[8,11,12,15] which is in good accordance with the XPS analyses. Furthermore, the extended X-ray absorption fine structure (EXAFS) spectrum of the $Ni_3GaC_{0.5}$ catalyst shows an obvious scattering peak at 1.7 Å,[26] which is assigned to the formation of Ni–C coordination in Fig. 3d. Besides, the Ni–Ni (Ga) scattering peak at 2.1 Å of $Ni_3GaC_{0.5}$ shifts slightly to a longer radial distance than those of the Ni and Ni_3Ga catalysts. The EXAFS oscillations at the K edge of these Ni catalysts in the ESI, Fig. S12† reveal that the $Ni_3GaC_{0.5}$ catalyst displays shorter periods and smaller amplitudes than the Ni_3Ga and Ni catalysts, demonstrating the longer coordination distance of Ni–Ni (Ga) and lower coordination environment in the $Ni_3GaC_{0.5}$ catalyst.[39–42] Wavelet transform (WT) analyses of the Ni EXAFS oscillations were further carried out to confirm the formation of Ni–C coordination in the $Ni_3GaC_{0.5}$ catalyst (Fig. 3e). The WT-EXAFS contour plots of these catalysts exhibit a maximum at around 8.1 Å^{-1} contributed by the Ni–Ni (Ga) coordination. Moreover, the WT-EXAFS contour plot of the $Ni_3GaC_{0.5}$ catalyst shows a maximum at around 4.5 Å^{-1}, which is ascribed to the contribution of the Ni–C coordination. The curve fitting results of all three Ni-based catalysts are shown in the ESI, Fig. S13–S15 and Table S1,† which also reveal the presence of Ni–C coordination in the $Ni_3GaC_{0.5}$ catalyst.

The electronic structures of Ni_3Ga and $Ni_3GaC_{0.5}$ catalysts were then studied by DFT calculations. Based on the Wulff construction crystals for Ni, Ni_3Ga and $Ni_3GaC_{0.5}$ in the ESI, Fig. S16,† the thermodynamically stable and mostly exposed surfaces, *i.e.*, Ni(111), Ni_3Ga(111) and $Ni_3GaC_{0.5}$(111) surfaces, were selected for the model calculations. The configurations of these surfaces are schematically shown in the ESI, Fig. S17.† Bader charge density difference analyses on the Ni_3Ga(111) and $Ni_3GaC_{0.5}$(111) surfaces were employed to reveal the changes in the electronic structure after doping C atoms into the lattice of Ni_3Ga. Fig. 4a and S18† exhibit distinct charge transfer from Ni

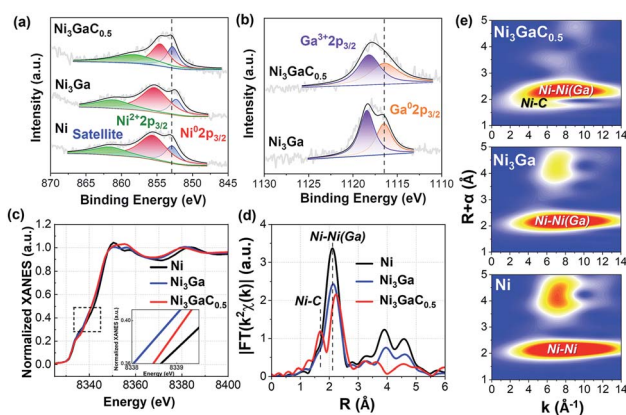**Fig. 3** (a) Ni 2p and (b) Ga 2p XPS spectra of Ni, Ni_3Ga and $Ni_3GaC_{0.5}$ catalysts. (c) Normalized XANES spectra at the Ni K-edge of Ni, Ni_3Ga and $Ni_3GaC_{0.5}$ catalysts. (d) Fourier transforms of the experimental EXAFS spectra of Ni, Ni_3Ga and $Ni_3GaC_{0.5}$ catalysts. (e) WT-EXAFS of the Ni K-edge signal for Ni, Ni_3Ga and $Ni_3GaC_{0.5}$ catalysts.

19726 | *J. Mater. Chem. A*, 2022, **10**, 19722–19731

This journal is © The Royal Society of Chemistry 2022

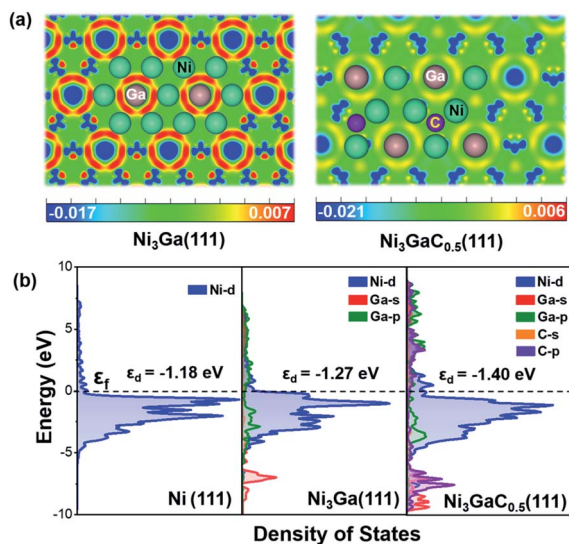**Fig. 4** (a)Two dimensional contours of the charge density difference of $Ni_3Ga(111)$ and $Ni_3GaC_{0.5}(111)$ surfaces, where the units of the color bars are e bohr^{-3}. (b) Projected electronic densities of states of the C p and s orbitals, Ga p and s orbitals, and those of the Ni d orbitals on Ni(111), $Ni_3Ga(111)$ and $Ni_3GaC_{0.5}(111)$ surfaces.

Fig. 5 (a) C_2H_2 conversion and (b) C_2H_4 selectivity as a function of reaction temperature. (c) Comparison for acetylene conversion and product selectivities of the Ni, Ni_3Ga and $Ni_3GaC_{0.5}$ catalysts. (d) Acetylene conversion and (e) ethylene selectivity with time on stream over the Ni, Ni_3Ga and $Ni_3GaC_{0.5}$ catalysts.

atoms to the C atoms underneath these Ni atoms, which is well consistent with the above XPS and XANES analyses. As further revealed by the density of states (DOS) profiles (Fig. 4b), the d-band of Ni atoms overlaps with the p-bands of Ga and C atoms in $Ni_3GaC_{0.5}$, suggesting obvious hybridization of Ni 3d with Ga 2p and C 2p orbitals, especially the hybridization of Ni 3d with Ga 2p orbitals. The hybridizations result in clear electron transfer from Ga atoms to Ni ones and then from Ni atoms to C ones. Moreover, the d-band centre of Ni on the $Ni_3GaC_{0.5}(111)$ surface downshifts toward lower energy compared with those on the Ni(111) and $Ni_3Ga(111)$ surfaces. These indicate that the introduction of C atoms into the Ni_3Ga lattice could effectively weaken the interaction between ethylene and Ni active sites and thus favour the desorption against its hydrogenation. Thus, the acetylene semi-hydrogenation would be enhanced on the $Ni_3GaC_{0.5}$ catalyst due to the synergistic modifications of Ga and subsurface C onto the Ni active sites.

The catalytic performance of the fabricated $Ni_3GaC_{0.5}$ catalyst was evaluated for acetylene semi-hydrogenation in excess ethylene in comparison with those of the Ni and Ni_3Ga catalysts. Fig. 5a, b, S19 and S20† show the conversion of acetylene as well as the selectivity to ethylene, ethane and C_4 products on the Ni, Ni_3Ga and $Ni_3GaC_{0.5}$ catalysts, respectively. The Ni catalyst exhibits significant over-hydrogenation and coupling performance for acetylene and thus leads to obvious formation of ethane and C_4 products (Fig. S19 and S20†), respectively. Notably, the negative ethylene selectivity on the Ni catalyst indicates the hydrogenation of ethylene contained in the reactant mixture. In contrast, the over-hydrogenation and coupling processes are suppressed on the Ni_3Ga intermetallic, due to the partial isolation of Ni sites by Ga and electronic interaction between Ni and Ga.[8] However, the performance on the Ni_3Ga

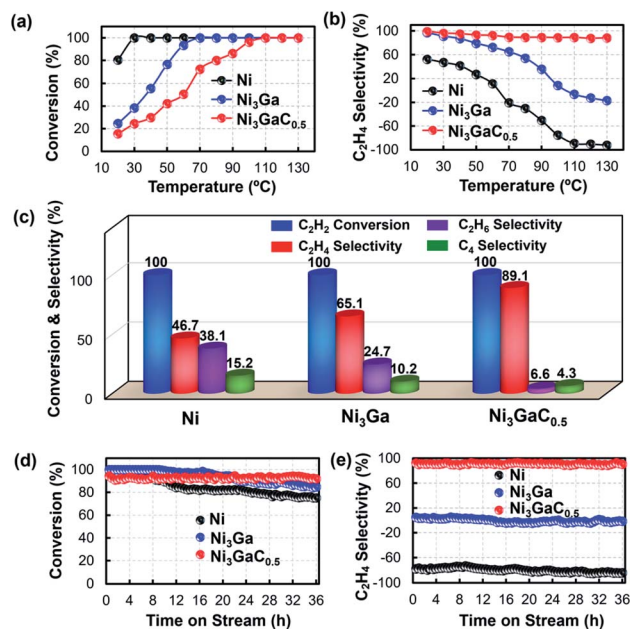catalyst is not good enough for acetylene semi-hydrogenation. Further incorporation of C atoms in Ni_3Ga forming the $Ni_3GaC_{0.5}$ catalyst results in much higher selectivity to the target ethylene product compared to Ni and Ni_3Ga catalysts in the temperature range from 20 to 130 °C, probably due to the favoured desorption of ethylene as predicted by the DOS analysis. In addition, the over-hydrogenation of acetylene to ethane and the coupling to C_4 products are remarkably suppressed on the $Ni_3GaC_{0.5}$ catalyst (Fig. S19 and S20†). As clearly shown in Fig. 5c, the $Ni_3GaC_{0.5}$ catalyst exhibits an extraordinary ethylene selectivity of 89.1% even at full acetylene conversion, with only 6.6% of ethane selectivity and 4.3% of C_4 selectivity. However, the Ni and Ni_3Ga catalysts exhibit much lower ethylene selectivity of 46.7% and 65.1% at the full conversion of acetylene, respectively. Moreover, the selectivities to C_4 products on the Ni and Ni_3Ga catalysts are 15.2% and 10.2%, significantly higher than that on the $Ni_3GaC_{0.5}$ catalyst. Thus, the catalytic performance of the $Ni_3GaC_{0.5}$ catalyst is more promising than those of the Ni and Ni_3Ga catalysts as well as previously reported Ni-based catalysts (Table 1).

The differences in the selectivity to C_4 products on these catalysts indicate the different stabilities of the Ni, Ni_3Ga and $Ni_3GaC_{0.5}$ catalysts. Therefore, stability tests were further carried out for the Ni, Ni_3Ga and $Ni_3GaC_{0.5}$ catalysts in the presence of excess ethylene. As shown in Fig. 5d, e, S21 and S22,† the conversions of acetylene on the Ni and Ni_3Ga catalysts decrease gradually with time on stream, showing poor catalytic stability. This could be ascribed to the accumulation of green oil on the catalysts due to the coupling of acetylene. Moreover, the selectivities to ethylene on the Ni and Ni_3Ga catalysts also

Table 1 Comparison of the catalytic performances of the Ni-based catalysts for acetylene semi-hydrogenation

Catalysts	Acetylene conversion (%)	Temperature (°C)	Reaction time (h)	Ethylene selectivity (%)	Ethylene selectivity[a] (%)	Reactants
Ni/SiO_2 (ref. 43)	40	180	36	50	—	$C_2H_2 + H_2$
Ni/SiO_2–Al_2O_3 (ref. 44)	<8	175	3	70–80	—	$C_2H_2 + H_2$
$NiGa/MgAl_2O_4$ (ref. 8)	93	190	24	78	78	$C_2H_2 + C_2H_4 + H_2$
Ni_3Ga[10]	92	200	24	77	77	$C_2H_2 + C_2H_4 + H_2$
$Ni_3GaC_{0.5}$ (this work)	100	110	36	90	90	$C_2H_2 + C_2H_4 + H_2$
$Ni_{10}In/SiO_2$ (ref. 43)	100	180	36	60	60	$C_2H_2 + H_2$
$AgNi_{0.125}/SiO_2$ (ref. 45)	90.4	160	—	31.4	31.4	$C_2H_2 + C_2H_4 + H_2$
Ni_5Zn_{21} (ref. 46)	75	160	12	50	50	$C_2H_2 + C_2H_4 + H_2$
$NiZn_2/MgAl_2O_4$ (ref. 47)	75	120	—	60	50	$C_2H_2 + H_2$
Pre-NiCu/MMO[4]	60	150	20	—	70	$C_2H_2 + C_2H_4 + H_2$
$Cu_{2.75}Ni_{0.25}Fe$[48]	100	250	5	75	75	$C_2H_2 + C_2H_4 + H_2$
Ni_3Sn_2 (ref. 10)	76	200	24	80	80	$C_2H_2 + C_2H_4 + H_2$
$Ni_3ZnC_{0.7}/C$[49]	100	165	10	85	85	$C_2H_2 + H_2$
Ni_1MoS/Al_2O_3 (ref. 25)	100	120	16	90	90	$C_2H_2 + C_2H_4 + H_2$
Ni_1/g-C_3N_4 (ref. 1)	30	260	50	85	85	$C_2H_4 + C_2H_4 + H_2$
Ni_1Cu_2/g-C_3N_4 (ref. 1)	100	160	350	90	90	$C_2H_2 + C_2H_4 + H_2$

[a] Ethylene selectivity at acetylene conversion higher than 90%.

decrease slightly with the time on stream while those to ethane and C_4 products increase slightly, which implies that the deposition of green oil is unfavourable for the semi-hydrogenation. Differently, the acetylene conversion on the $Ni_3GaC_{0.5}$ catalyst remains steady at 91.3% through the 36 hour stability test, and the selectivity toward ethylene could be maintained at 90.1% without legible decline, which are both superior to the Ni and Ni_3Ga catalysts. All the above results unambiguously demonstrate that the $Ni_3GaC_{0.5}$ catalyst exhibits superior performance for the acetylene semi-hydrogenation.

The difference in the stabilities of Ni, Ni_3Ga and $Ni_3GaC_{0.5}$ catalysts is explored by the thermogravimetric-differential thermal analysis (TG-DTG) and pyrolysis gas chromatography-

mass spectrometer (GC-MS) measurements. As shown in Fig. 6a, the weight loss of the spent $Ni_3GaC_{0.5}$ catalyst (about 2.6 wt%), attributed to the oxidative decomposition of green oil, is lower than those of the spent Ni and Ni_3Ga catalysts. Besides, in the DTG curves, the main peak clearly observed for the spent $Ni_3GaC_{0.5}$ catalyst shifts toward lower temperature in comparison with those of the Ni and Ni_3Ga catalysts, which indicates that the small amount of hydrocarbons accumulated on the spent $Ni_3GaC_{0.5}$ catalyst are lighter than those on the Ni and Ni_3Ga catalysts.[4,5,8]

The main composition of green oil formed on the used Ni, Ni_3Ga and $Ni_3GaC_{0.5}$ catalysts is determined by pyrolysis GC-MS and shown in Fig. 6b. The result of pyrolysis GC-MS analysis of a standard sample completely mixed with various chain hydrocarbons is also included to identify the components in the green oil. The main intensities of peaks observed on the spent Ni and Ni_3Ga catalysts are much stronger than those for the used $Ni_3GaC_{0.5}$ catalyst, indicating that more considerable green oil was accumulated on the Ni and Ni_3Ga catalysts than on the $Ni_3GaC_{0.5}$ catalyst. More importantly, it can be obviously seen from Fig. 6c that the green oil accumulated on Ni and Ni_3Ga catalysts contains more heavy hydrocarbons than those on the $Ni_3GaC_{0.5}$ catalyst, which is also revealed by the statistical average carbon number of the components contained in the green oil for the used Ni, Ni_3Ga and $Ni_3GaC_{0.5}$ catalysts. These clearly reveal that the formation of green oil on the $Ni_3GaC_{0.5}$ catalyst is restrained as compared to those on the Ni and Ni_3Ga catalysts.

DFT calculations were performed to gain more mechanistic insights into the boosted acetylene semi-hydrogenation on the $Ni_3GaC_{0.5}$ catalyst with the incorporation of C atoms in the lattice. As shown in Fig. 7a and Tables S2, S3,† the adsorption of C_2H_2 and C_2H_4 on the $Ni_3GaC_{0.5}$(111) surface is energetically favourable through the di-σ configurations with moderate adsorption free energies of −1.71 and −0.69 eV, respectively. In contrast, the adsorption free energies of acetylene and ethylene
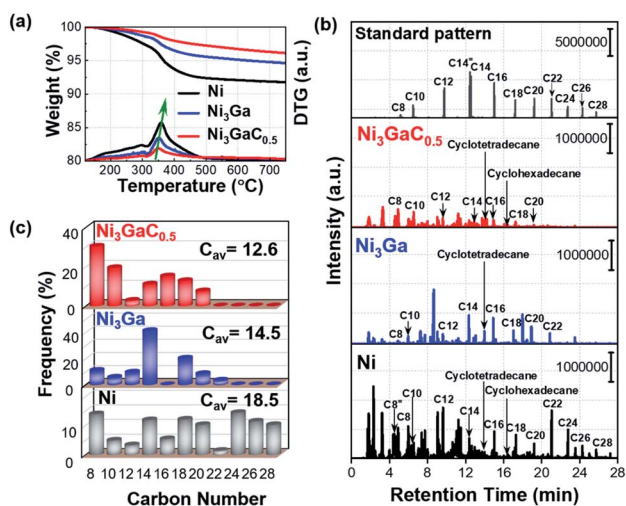

Fig. 6 (a) TG-DTG profiles of the spent Ni, Ni_3Ga and $Ni_3GaC_{0.5}$ catalysts. (b) Pyrolysis GC-MS profiles of green oil deposited on the Ni, Ni_3Ga and $Ni_3GaC_{0.5}$ catalysts and (c) corresponding statistics for carbon numbers of hydrocarbons contained in green oil.
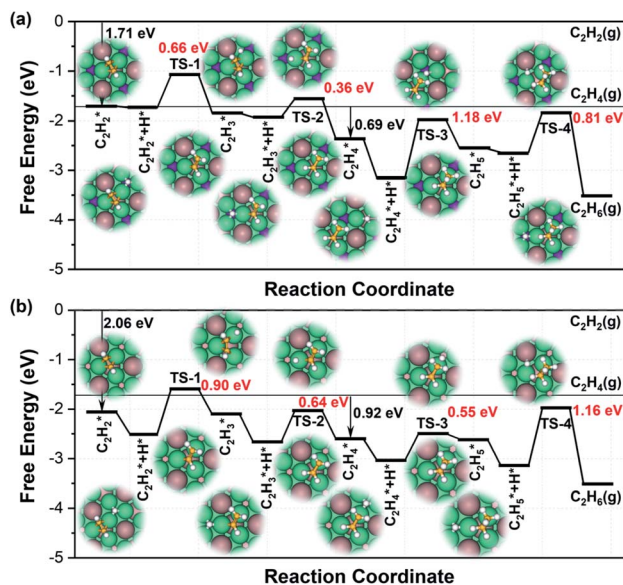
19728 | J. Mater. Chem. A, 2022, **10**, 19722–19731

This journal is © The Royal Society of Chemistry 2022

Fig. 7 Free energy profiles for acetylene hydrogenation on the (a) $Ni_3GaC_{0.5}(111)$ and (b) $Ni_3Ga(111)$ surfaces. Numbers in the above reaction pathways suggest the free energy barriers of elementary steps; Ni, green; Ga: brown; subsurface C: purple; C: yellow; H: white.

increase in the order of $Ni_3GaC_{0.5}(111) < Ni_3Ga(111) < Ni(111)$ (Tables S2–S7†), which is in good accordance with the predictions of the DOS analyses. The calculated free energy barriers of the initial two hydrogenation steps from C_2H_2 to C_2H_4 over the $Ni_3GaC_{0.5}(111)$ surface are 0.66 and 0.36 eV with exothermic energies of 0.76 and 0.81 eV, respectively, indicating the decent hydrogenation activity of acetylene. The effective energy barrier (G_a^{eff}) is employed to further compare the differences in the hydrogenation activities on Ni, Ni_3Ga and $Ni_3GaC_{0.5}$, and the lower G_a^{eff} indicates higher activity.[50,51] More details on the calculation of G_a^{eff} are presented in the ESI, Fig. S23–S26 and Table S10.† The values of G_a^{eff} on the Ni(111), $Ni_3Ga(111)$ and $Ni_3GaC_{0.5}(111)$ surfaces are 1.19, 1.35 and 1.67 eV, respectively, which suggest that the hydrogenation activity decreases in the order Ni > Ni_3Ga > $Ni_3GaC_{0.5}$. The kinetics studies on these catalysts also reveal that the apparent activation energy for acetylene hydrogenation on the Ni, Ni_3Ga and $Ni_3GaC_{0.5}$ catalysts also increases in the order Ni < Ni_3Ga < $Ni_3GaC_{0.5}$ (Fig. S27†), which is in good accordance with the DFT results. The free energy barrier for further hydrogenation of the formed C_2H_4 species to C_2H_5 on the $Ni_3GaC_{0.5}$ (111) surface is calculated to be 1.18 eV, which is obviously higher than the desorption free energy of C_2H_4 (i.e., 0.69 eV). This energetics comparison demonstrates that the formed C_2H_4 species prefers to desorb from the surface rather than to be hydrogenated,[8,17] highlighting the excellent selectivity to ethylene. Similar results are also seen on the sub-stable $Ni_3GaC_{0.5}(200)$ surface, on which the free energy barrier for further hydrogenation of the formed C_2H_4 species to C_2H_5 is clearly higher than that for ethylene desorption (Fig. S30, Tables S9 and S11†).

For comparison, the hydrogenation of acetylene over the Ni(111) and $Ni_3Ga(111)$ surfaces was also investigated. As seen

in Fig. 7b, the free energy barriers for the conversion of C_2H_2 to C_2H_4 via two-step hydrogenations on the $Ni_3Ga(111)$ surface are 0.90 and 0.64 eV with exothermic energies of 0.51 and 0.57 eV, respectively. Notably, the free energy barrier for the hydrogenation of the formed C_2H_4 species is 0.55 eV, much lower than its desorption free energy, which reveals that ethylene on the $Ni_3Ga(111)$ surface is prone to hydrogenation to the undesired ethane before desorption. On the sub-stable $Ni_3Ga(200)$ surface, the hydrogenation of ethylene is also demonstrated to be more favorable than the desorption of ethylene (Fig. S29, Tables S8 and S11†). As shown in the ESI, Fig. S28,† similar results are also seen with the Ni(111) surface, on which the free energy barrier for the hydrogenation of C_2H_4 (i.e., 0.42 eV) is clearly lower than the desorption free energy (i.e., 0.82 eV). These results are well consistent with the remarkably lower selectivity to ethylene on the Ni and Ni_3Ga catalysts than on the $Ni_3GaC_{0.5}$ catalyst (Fig. 5b).

4.   Conclusion

In summary, acetylene reactant has been employed to thermally process the Ni_3Ga intermetallic catalyst in order to introduce subsurface carbon atoms to promote the activity of the Ni_3Ga catalyst toward acetylene semi-hydrogenation. The processed Ni_3Ga intermetallic catalyst is proven to show the typical $Ni_3GaC_{0.5}$ structure by XRD, AC-HAADF-STEM and XAS measurements. The presence of subsurface carbon is experimentally and theoretically demonstrated to synergize with Ga sites for modifying the structures of Ni sites in the $Ni_3GaC_{0.5}$ catalyst, especially the electronic structures of Ni, which contributes to moderate adsorption of the acetylene reactant and simultaneously weak adsorption of ethylene product. The catalytic performance tests show that the $Ni_3GaC_{0.5}$ catalyst displays excellent performance for acetylene semi-hydrogenation, with ethylene selectivity up to ca. 90% at full conversion of acetylene, outperforming the referred Ni and Ni_3Ga catalysts. The excellent selectivity to ethylene is rationalized by DFT calculations, which point out that the desorption of ethylene from the $Ni_3GaC_{0.5}$ catalyst is kinetically more favourable than its hydrogenation to ethane. Moreover, due to the suppressed formation of C_4 products, the stability of the $Ni_3GaC_{0.5}$ catalyst is also enhanced against the Ni and Ni_3Ga catalysts. This work exemplifies the possibility of regulating active sites by subsurface dopants synergized with surface ones toward enhanced selectivity to the target products in heterogeneous catalysis, which could provide a new avenue for designing and optimizing the catalysts.

Author contributions

XG and ZR performed the experiments, conducted the density functional theory calculation, collected the data, and wrote the paper. YC and XD conceived this work, designed the research, supervised the experiments, and edited the paper. ZR conducted the AC-HAADF-STEM tests under the supervision of XL and LC. JZ, GQ, XZ and WY helped with data analyses and

discussions. All the authors contributed to the manuscript revisions.

Conflicts of interest

There are no conflicts to declare.

Acknowledgements

Notes and references

1 J. Gu, M. Jian, L. Huang, Z. Sun, A. Li, Y. Pan, J. Yang, W. Wen, W. Zhou, Y. Lin, H. J. Wang, X. Liu, L. Wang, X. Shi, X. Huang, L. Cao, S. Chen, X. Zheng, H. Pan, J. Zhu, S. Wei, W. X. Li and J. Lu, *Nat. Nanotechnol.*, 2021, **16**, 1141–1149.

2 R. Gao, J. Xu, J. Wang, J. Lim, C. Peng, L. Pan, X. Zhang, H. Yang and J. J. Zou, *J. Am. Chem. Soc.*, 2021, **144**, 573–581.

3 A. Wang, J. Li and T. Zhang, *Nat. Rev. Chem.*, 2018, **2**, 65–81.

4 Y. Liu, J. Zhao, J. Feng, Y. He, Y. Du and D. Li, *J. Catal.*, 2018, **359**, 251–260.

5 Y. Cao, Z. Sui, Y. Zhu, X. Zhou and D. Chen, *ACS Catal.*, 2017, **7**, 7835–7846.

6 Y. Niu, X. Huang, Y. Wang, M. Xu, J. Chen, S. Xu, M. G. Willinger, W. Zhang, M. Wei and B. Zhang, *Nat. Commun.*, 2020, **11**, 3324.

7 F. Studt, F. Abild-Pedersen, T. Bligaard, R. Z. Sørensen, C. H. Christensen and J. K. Nørskov, *Science*, 2008, **320**, 1320–1322.

8 Y. Cao, H. Zhang, S. Ji, Z. Sui, Z. Jiang, D. Wang, F. Zaera, X. Zhou, X. Duan and Y. Li, *Angew. Chem., Int. Ed.*, 2020, **59**, 11647–11652.

9 Y. Chai, G. Wu, X. Liu, Y. Ren, W. Dai, C. Wang, Z. Xie, N. Guan and L. Li, *J. Am. Chem. Soc.*, 2019, **141**, 9920–9927.

10 Y. Liu, X. Liu, Q. Feng, D. He, L. Zhang, C. Lian, R. Shen, G. Zhao, Y. Ji, D. Wang, G. Zhou and Y. Li, *Adv. Mater.*, 2016, **28**, 4747–4754.

11 J. Yu, Y. Yang, L. Chen, Z. Li, W. Liu, E. Xu, Y. Zhang, S. Hong, X. Zhang and M. Wei, *Appl. Catal., B*, 2020, **277**, 119273–119281.

12 W. Liu, Y. Yang, L. Chen, E. Xu, J. Xu, S. Hong, X. Zhang and M. Wei, *Appl. Catal., B*, 2021, **282**, 119569–119579.

13 L. Zhang, M. Zhou, A. Wang and T. Zhang, *Chem. Rev.*, 2020, **120**, 683–733.

14 M. Zhou, C. Li and J. Fang, *Chem. Rev.*, 2021, **121**, 736–795.

15 C. Li, Y. Chen, S. Zhang, S. Xu, J. Zhou, F. Wang, M. Wei, D. G. Evans and X. Duan, *Chem. Mater.*, 2013, **25**, 3888–3896.

16 D. M. Rao, S. T. Zhang, C. M. Li, Y. D. Chen, M. Pu, H. Yan and M. Wei, *Dalton Trans.*, 2018, **47**, 4198–4208.

17 Q. Feng, S. Zhao, Y. Wang, J. Dong, W. Chen, D. He, D. Wang, J. Yang, Y. Zhu, H. Zhu, L. Gu, Z. Li, Y. Liu, R. Yu, J. Li and Y. Li, *J. Am. Chem. Soc.*, 2017, **139**, 7294–7301.

18 H. Zhou, X. Yang, L. Li, X. Liu, Y. Huang, X. Pan, A. Wang, J. Li and T. Zhang, *ACS Catal.*, 2016, **6**, 1054–1061.

19 B. Lou, H. Kang, W. Yuan, L. Ma, W. Huang, Y. Wang, Z. Jiang, Y. Du, S. Zou and J. Fan, *ACS Catal.*, 2021, **11**, 6073–6080.

20 M. Jorgensen and H. Gronbeck, *J. Am. Chem. Soc.*, 2019, **141**, 8541–8549.

21 S. Zhou, L. Shang, Y. Zhao, R. Shi, G. I. N. Waterhouse, Y. C. Huang, L. Zheng and T. Zhang, *Adv. Mater.*, 2019, **31**, e1900509.

22 F. Huang, Y. Deng, Y. Chen, X. Cai, M. Peng, Z. Jia, P. Ren, D. Xiao, X. Wen, N. Wang, H. Liu and D. Ma, *J. Am. Chem. Soc.*, 2018, **140**, 13142–13146.

23 M. R. Ball, K. R. Rivera-Dones, E. B. Gilcher, S. F. Ausman, C. W. Hullfish, E. A. Lebrón and J. A. Dumesic, *ACS Catal.*, 2020, **10**, 8567–8581.

24 S. Zou, B. Lou, K. Yang, W. Yuan, C. Zhu, Y. Zhu, Y. Du, L. Lu, J. Liu, W. Huang, B. Yang, Z. Gong, Y. Cui, Y. Wang, L. Ma, J. Ma, Z. Jiang, L. Xiao and J. Fan, *Nat. Commun.*, 2021, **12**, 5770.

25 B. Fu, A. J. McCue, Y. Liu, S. Weng, Y. Song, Y. He, J. Feng and D. Li, *ACS Catal.*, 2021, 607–615, DOI: 10.1021/ acscatal.1c04758.

26 K. Y. Kim, J. H. Lee, H. Lee, W. Y. Noh, E. H. Kim, E. C. Ra, S. K. Kim, K. An and J. S. Lee, *ACS Catal.*, 2021, **11**, 11091– 11102.

27 D. Teschner, J. Borsodi, A. Wootsch, Z. Révay, M. Hävecker, A. Knop-Gericke, S. D. Jackson and R. Schlögl, *Science*, 2008, **320**, 86–89.

28 C. W. Chan, A. H. Mahadi, M. M. Li, E. C. Corbos, C. Tang, G. Jones, W. C. Kuo, J. Cookson, C. M. Brown, P. T. Bishop and S. C. Tsang, *Nat. Commun.*, 2014, **5**, 5787.

29 J. Zhang, Z. Sui, Y.-A. Zhu, D. Chen, X. Zhou and W. Yuan, *Chem. Eng. Technol.*, 2016, **39**, 865–873.

30 G. Kresse and J. Furthmüller, *Comput. Mater. Sci.*, 1996, **6**, 15–50.

31 G. Kresse and J. Furthmüller, *Phys. Rev. B: Condens. Matter Mater. Phys.*, 1996, **54**, 11169–11186.

32 G. Kresse and D. Joubert, *Phys. Rev. B: Condens. Matter Mater. Phys.*, 1999, **59**, 1758–1775.

33 P. E. Blochl, *Phys. Rev. B: Condens. Matter Mater. Phys.*, 1994, **50**, 17953–17979.

34 J. P. Perdew, K. Burke and M. Ernzerhof, *Phys. Rev. Lett.*, 1996, **77**, 3865–3868.

35 J. Kastner and P. Sherwood, *J. Chem. Phys.*, 2008, **128**, 014106.

36 W. Tang, E. Sanville and G. Henkelman, *J. Phys.: Condens. Matter*, 2009, **21**, 084204.

37 Y. Cao, X. Ge, Y. Li, R. Si, Z. Sui, J. Zhou, X. Duan and X. Zhou, *Engineering*, 2021, **7**, 103–110.

19730 | *J. Mater. Chem. A*, 2022, **10**, 19722–19731

This journal is © The Royal Society of Chemistry 2022

38 G. Fan, W. Xu, J. Li, J. L. Chen, M. Yu, Y. Ni, S. Zhu, X. C. Su and F. Cheng, *Adv. Mater.*, 2021, **33**, e2101126.

39 J. E. Penner-Hahn, *Coord. Chem. Rev.*, 1999, **190–192**, 1101–1123.

40 J. J. Rehr and R. C. Albers, *Rev. Mod. Phys.*, 2000, **72**, 621–654.

41 A. I. Frenkel, A. Yevick, C. Cooper and R. Vasic, *Annu. Rev. Anal. Chem.*, 2011, **4**, 23–39.

42 A. I. Frenkel, *Chem. Soc. Rev.*, 2012, **41**, 8163–8178.

43 Y. Chen and J. Chen, *Appl. Surf. Sci.*, 2016, **387**, 16–27.

44 C. Guimon, *Appl. Catal., A*, 2003, **251**, 199–214.

45 G. X. Pei, X. Y. Liu, A. Wang, Y. Su, L. Li and T. Zhang, *Appl. Catal., A*, 2017, **545**, 90–96.

46 C. S. Spanjers, J. T. Held, M. J. Jones, D. D. Stanley, R. S. Sim, M. J. Janik and R. M. Rioux, *J. Catal.*, 2014, **316**, 164–173.

47 D. L. Trimm, N. W. Cant and I. O. Y. Liu, *Catal. Today*, 2011, **178**, 181–186.

48 B. Bridier and J. Pérez-Ramírez, *J. Am. Chem. Soc.*, 2010, **132**, 4321–4327.

49 Y. Wang, B. Liu, X. Lan and T. Wang, *ACS Catal.*, 2021, **11**, 10257–10266.

50 S. Kozuch and J. M. L. Martin, *ACS Catal.*, 2011, **1**, 246–253.

51 S. Kozuch and S. Shaik, *Acc. Chem. Res.*, 2011, **44**, 101–110.

This journal is © The Royal Society of Chemistry 2022

J. Mater. Chem. A, 2022, **10**, 19722–19731 | **19731**